J Physiol 592.6 (2014) pp 1249–1266

The Journal of Physiology

Vasoactive agonists exert dynamic and coordinated effects on vascular smooth muscle cell elasticity, cytoskeletal remodelling and adhesion

Zhongkui Hong[1], Zhe Sun[1], Min Li[1], Zhaohui Li[1], Filiz Bunyak[2], Ilker Ersoy[2], Jerome P. Trzeciakowski[3], Marius Catalin Staiculescu[1], Minshan Jin[1], Luis Martinez-Lemus[1,4], Michael A. Hill[1,4], Kannappan Palaniappan[2] and Gerald A. Meininger[1,4]

[1] *Dalton Cardiovascular Research Center,* [2] *Department of Computer Science, and* [4] *Department of Pharmacology and Physiology, University of Missouri, Columbia, MO, USA*

[3] *Department of Systems Biology, Texas A&M University, College Station, TX, USA*

Key points

- This study demonstrates rapid and dynamic changes in adhesion and cell elasticity following agonist stimulation that culminate in a remodelled cytoskeleton in vascular smooth muscle.
- Evidence is presented that the changes in adhesion and elasticity are coordinated and that these variables demonstrate temporal oscillation consisting of three major oscillation components.
- Eigen-decomposition spectrum analysis revealed that these components of oscillation in cell elasticity and adhesion may be linked by shared signalling pathways.
- Evidence is provided that the agonists angiotensin II and adenosine produce remodelling of actin cytoskeleton that may alter the properties of the observed oscillations in elasticity and adhesion.
- It is concluded that angiotensin II and adenosine may regulate extracellular matrix adhesion and elasticity in vascular smooth muscle cells as a form of adaptation to more efficiently support contractile behaviour.

Abstract In this study, we examined the ability of vasoactive agonists to induce dynamic changes in vascular smooth muscle cell (VSMC) elasticity and adhesion, and tested the hypothesis that these events are coordinated with rapid remodelling of the cortical cytoskeleton. Real-time measurement of cell elasticity was performed with atomic force microscopy (AFM) and adhesion was assessed with AFM probes coated with fibronectin (FN). Temporal data were analysed using an Eigen-decomposition method. Elasticity in VSMCs displayed temporal oscillations with three components at approximately 0.001, 0.004 and 0.07 Hz, respectively. Similarly, adhesion displayed a similar oscillatory pattern. Angiotensin II (ANG II, 10^{-6} M) increased (+100%) the amplitude of the oscillations, whereas the vasodilator adenosine (ADO, 10^{-4} M) reduced oscillation amplitude (–30%). To test whether the oscillatory changes were related to the architectural alterations in cortical cytoskeleton, the topography of the submembranous actin cytoskeleton (100–300 nm depth) was acquired with AFM. These data were analysed to compare cortical actin fibre distribution and orientation before and after treatment with vasoactive agonists. The results showed that ANG II increased the density of stress fibres by 23%, while ADO decreased the density of the stress fibres by 45%. AFM data were supported by Western blot and confocal microscopy. Collectively, these observations indicate that VSMC cytoskeletal structure and adhesion to the extracellular matrix are dynamically altered in response to agonist stimulation. Thus, vasoactive agonists probably invoke unique mechanisms that dynamically alter the behaviour and structure of both the VSMC cytoskeleton and focal adhesions to efficiently support the normal contractile behaviour of VSMCs.

DOI: 10.1113/jphysiol.2013.264929

(Received 11 September 2013; accepted after revision 15 January 2014; first published online 20 January 2014)
Corresponding author G. A. Meininger: Dalton Cardiovascular Center, University of Missouri, 134 Research Park Dr., Columbia, MO 65211, USA. Email: meiningerg@missouri.edu

Abbreviations ADO, adenosine; AFM, atomic force microscopy; ANG II, angiotensin II; ECM, extracellular matrix; eLoG, elongated Laplacian of Gaussian; *E*-modulus, Young's modulus; FBS, fetal bovine serum; FN, fibronectin; GFP, green fluorescent protein; JSP, jasplakinolide; LAT-A, latrunculin A; PBS, phosphate-buffered saline; PEG, polyethylene glycol; VSMC, vascular smooth muscle cell.

Introduction

Vascular smooth muscle cells (VSMCs) represent dynamic systems constantly changing their shape and architecture through the coordinated rearrangement of cellular components and position within the vascular wall to adapt to alterations in their chemical and mechanical environments (Martinez-Lemus *et al.* 2009). In a previous study, we reported an acute vascular remodelling of arterioles acutely exposed to noradrenaline (norepinephrine) which was characterized by repositioning of VSMCs within the vascular wall (Martinez-Lemus *et al.* 2004). This structural remodelling of the vascular wall was viewed as a mechanoadaptive process providing a potentially mechanical and energy efficient means of maintaining a chronic constriction.

In VSMCs the cytoskeleton is the major cellular component that generates forces and motion related to contraction. Importantly, the elasticity of the cytoskeleton is known to resist deforming forces caused by changes in extracellular mechanical events acting on the cell (Fletcher & Mullins, 2010). In many cell types, cytoskeletal reorganization can dynamically alter cellular architecture to allow for changes in cell shape, cell movement and contraction in response to a variety of chemical and mechanical stimuli (Adams, 1992; Hale *et al.* 2010). It is now known that there are both contractile and non-contractile cytoskeletal compartments (Parker *et al.* 1998; De Deyne, 2001; Kim *et al.* 2008; Dowling *et al.* 2012). These two compartments have been suggested to interact to orchestrate smooth muscle cell contraction and maintenance of cell rigidity during contraction. These interactions are dynamic and driven by changes in cytoskeletal architecture and activity of molecular motors (Jülicher & Prost, 1997; Martens & Radmacher, 2008; Koenderink *et al.* 2009; Plaçais *et al.* 2009; Woolner & Bement, 2009; Sweeney & Houdusse, 2010) and it is realistic to propose that cytoskeletal changes are coordinated with changes in adhesion.

On the basis of the above, the goal of this study was to test the hypothesis that the contractile plasticity of VSMCs is a function of rapid remodelling of cell cytoskeletal structure and is adhesion driven, in part, by dynamic remodelling of the submembranous cytoskeleton. The dynamic nature of this process is supported by our previous studies showing temporal variation in VSMC cell elasticity and adhesion (Zhu *et al.* 2012). We further investigated the hypothesis that elasticity, cytoskeletal remodelling, and adhesion would be affected in opposite directions by vasoconstrictor and vasodilator agents. Collectively, these novel mechanisms may contribute to the adaptation of VSMCs in the vascular wall that occurs during cellular contraction and relaxation.

Methods

VSMC isolation and culture

Sprague–Dawley rats were used for this study and were maintained in accordance with the protocol of the *Guide for the Care and Use of Laboratory Animals* (NIH 83-23, revised 1996). The animal use in these studies was approved by the Laboratory Animal Use Committee of the University of Missouri. Briefly, 200–250 g rats were anaesthetized by ip injection of pentobarbitol sodium (Lundbeck, Inc., Deerfield, IL, USA) at 0.1 g/kg. The rat cremaster muscle was excised through a scrotal surgical incision while animal remained under anaesthesia. After dissection, the rat was euthanized immediately by intracardial injection of saturated KCl solution (3 ml), followed by bilateral pneumothorax. VSMCs were enzymatically isolated from the first-order arteriole (100–150 μm diameter) of rat cremaster skeletal muscles using previously described methods (Sun *et al.* 2008). Cells were maintained under culture conditions in Dulbecco's modified Eagle's medium/nutrient mixture F-12 (DMEM/F-12) supplemented with 10% fetal bovine serum (FBS) (Atlanta Biologicals, Lawrenceville, GA, USA), 10 mM HEPES (Sigma), 2 mM L–glutamine, 1 mM sodium pyruvate, 100 U ml^{-1} penicillin, and 100 μg ml^{-1} streptomycin. In preparation for experiments, cells were plated on 12 mm circular cover slips (Electron Microscopy Sciences, Hatfield, PA, USA) which were positioned in 12-well cell culture plates (Corning Inc., Corning, NY, USA) and kept in a humidified incubator (Heraeus Instruments, Newtown, CT, USA) with 5% CO_2 at 37°C. For AFM experiments, a single cover slip with cells was transferred to a 60 mm tissue culture dish (World Precision Instruments, Sarasota, FL, USA). The cells used in all AFM experiments were maintained in primary culture for 3–12 days without passage. Apart from HEPES and FBS, all reagents were purchased from Invitrogen (Carlsbad, CA, USA).

Fibronectin coating of AFM probes

A 5 μm diameter glass bead was glued on the tip of an AFM probe (all force measurement experiments in this study were performed with AFM probes acquired from Veeco: MLCT-O10, Santa Barbara, CA, USA; now supplied by Bruker Corp.) and then coated with fibronectin (FN; Sigma, St Louis, MO, USA) using the protocol described by Lehenkari & Horton (1999) and previously used in our laboratory (Sun *et al.* 2005; Qiu *et al.* 2010). Briefly, polyethylene glycol (PEG, Sigma) was used as a linker molecule between FN (Invitrogen) and the micro-bead. The probe was first incubated with 10 mM PEG (5 min), washed with phosphate-buffered saline (PBS), and then incubated with FN (0.25 mg ml^{-1}) for 5 min followed by rinsing with PBS. Each cantilever was calibrated after a given experiment using thermal noise amplitude analysis (Hutter & Bechhoefer, 1993; Butt & Jaschke, 1995). The measured spring constants were between 55 and 65 pN nm^{-1}.

Measurement of biomechanical properties with AFM

Monitoring of biomechanical properties of single live VSMCs in real time was performed using a Bioscope AFM System (Model IVa, Digital Instruments, Santa Barbara, CA, USA) that was mounted on an inverted microscope (Model IX81, Olympus America Inc.). All AFM measurements were conducted at room temperature (~25°C) in a serum-free medium without antibiotics. Prior to experiments cells were serum-starved overnight. We have previously shown that FN-coated AFM probes interact specifically with integrins. The binding is sensitive to inhibition with integrin-blocking antibodies and binding significantly exceeds non-specific ligands such as bovine serum albumin-coated probes (Sun *et al.* 2005). In this study the spherical AFM probe (5 μm in diameter) was coated with FN following same protocol as previously used to perform nano-indentation and retraction cycles on the cell surface and assess adhesion (Hong *et al.* 2012). The parameters employed were a 0.1 Hz sampling frequency, with an approach/retraction velocity of 320 nm s^{-1}, 3200 nm travelling distance for one sampling cycle (indentation and retraction), and approximately 1000–3000 pN loading force. Cells were randomly selected and indented at a site between the nucleus and cell margin to collect approximately 60 force curves within 20 min for a pre-drug period followed by 240 force curves over 40 min for the post-drug period. To minimize drift, after the probe was submerged in the cell bath, the AFM system was thermally and mechanically equilibrated for 1 h.

The analysis of force curves was automated using a proprietary software package (NForceR). For estimating Young's modulus (*E*-modulus) of the cell cortex, a length of approximately 100–300 nm of the AFM indentation curve, following the initial point of contact, was fitted with a modified Hertz model as shown in eqn (1) (Costa, 2003; Li *et al.* 2008):

$$E = \frac{3(1-\nu^2)}{4\sqrt{r_b}} \times \frac{F}{\delta^{\frac{3}{2}}} \quad (1)$$

where E is the E-modulus, F is the force exerted by the AFM probe on the cell surface, δ is the indentation depth into the cell membrane, r_b is the radius of the spherical AFM tip, and ν is the Poisson ratio for the cell. Cells were considered as a gel and the Poisson ratio ν was assumed to be 0.5 (Costa, 2003). The relationship between cell E-Modulus, indentation force, and indentation depth is illustrated in Figure S5. Adhesion forces between FN and integrin adhesion complexes were determined from the retraction curves as the product of the rupture height and cantilever spring constant.

AFM contact mode imaging

An atomic force microscope (model MFP-3D BIO; Asylum Research, Santa Barbara, CA, USA) mounted on an Olympus IX81 microscope was used in contact mode for the live cell topography imaging. The area of the cell surface that was scanned in these experiments was 40 μm × 40 μm and the digital density of the scanned area was 512 pixels × 512 pixels. A stylus-type AFM probe (model MLCT-C, $k = 15$ pN nm^{-1}, Bruker, Santa Barbara, CA, USA) was used to perform the cell surface scanning at 0.4 Hz frequency with a 300–500 pN tracking force at room temperature in DMEM/F12 medium without FBS supplementation. Height and deflection image data were collected with Asylum software and analysed using MATLAB (R2010b, MathWorks Inc., Natick, MA, USA).

Data processing and analysis of oscillations in cell elasticity and adhesion forces

A temporal spectral analysis procedure was developed for analysis and subsequent interpretation of the oscillatory waveforms observed over time in both the E-modulus and adhesion force data (Zhu *et al.* 2012). Singular spectral analysis, an Eigen-decomposition method, was used to isolate three primary oscillatory components for each time-series data set (Hassani, 2007) after linear trends were estimated. As described in our previous publication (Zhu *et al.* 2012), we visualized the average group behaviour of the oscillations through time-series analysis of amplitude, frequency and phase for each cell studied and then averaging these values over all cells. In this manner, a composite time series for each treatment set was reconstructed using eqn (2):

$$y(t) = \bar{A}_1 \sin(2\pi \bar{f}_1 t + \bar{\phi}_1) + \bar{A}_2 \sin(2\pi \bar{f}_2 t + \bar{\phi}_2) + \bar{A}_3 \sin(2\pi \bar{f}_3 t + \bar{\phi}_3) + \bar{b}_1 t + \bar{b}_0 \quad (2)$$

where b_1 and b_0 represent the slope and intercept of the linear trend, respectively, A_1, A_2 and A_3 the amplitude of the three components, f_1, f_2 and f_3 the oscillation frequency of the three components, ϕ_1, ϕ_2, and ϕ_3 the phase of the three components. The bar above each component represents the mean value.

The oscillations in adhesion force were analysed using methods described previously (Zhu *et al.* 2012). For each retraction the multiple individual rupture forces and the time points for each detected rupture event in the retraction force curve were obtained and incorporated into a time sequence by combination of probe retraction rate and the distance along the retraction curve at which a rupture event occurred. These data points were integral to the filter design in the MATLAB program and both influence the resulting smoothed fit of the data. The sampling rate of the raw data (Supporting information Fig. S1, available online) was irregular with an average frequency of 0.526 Hz. As nearly all signal analysis algorithms are based on regular constant intervals, an interpolation was performed by the MATLAB resample function using an anti-aliasing finite impulse response (FIR) filter to up-sample the raw data to 10 Hz while preserving the overall frequency response of the time series. In the second stage of the resample function these data were down-sampled to a regular sampling rate at 0.5 Hz. These resampled data points exactly followed the interpolated series of force and time data. After application of the resample function the interpolated data were then down-sampled to 0.1 Hz. Using this general approach the analysis routine could be adjusted to accommodate other sampling rates as well. To ensure equivalence, all measured time series (force, elasticity, contact point, displacement) were subjected to the same processing routines, even if the time points occurred at regular intervals (e.g. elasticity).

AFM image processing and stress fibre orientation and density analysis

The AFM deflection and height images were analysed with MATLAB as shown in the schematic illustration (Supporting information Fig. S2). The orientation and density of cytoskeletal filaments were determined using a novel method developed in our laboratory and combined with a modified method of Karlon (Karlon *et al.* 1999). Briefly, to evaluate the horizontal (G_x) and vertical (G_y) spatial gradients of whole pixels in AFM deflection images, two masks were computed with the following equations, (3) and (4), that were modified from the original algorithm (Karlon *et al.* 1999):

$$h_x(i,j) = \frac{2j}{\sigma^2} \times e^{\left[-\frac{i^2+j^2}{\sigma^2}\right]} \quad (3)$$

$$h_y(i,j) = \frac{2i}{\sigma^2} \times e^{\left[-\frac{i^2+j^2}{\sigma^2}\right]} \quad (4)$$

where h_x is the x direction mask, h_y is the y direction mask, and i and j represent the element position in row and column of the matrix, respectively. The standard deviation σ was considered as 3 in this study, and the masks were 13 pixels × 13 pixels in size. The 500 × 500 G_x and G_y were obtained by convolving the mask h_x *and* h_y to the original 512 × 512 deflection image pixel by pixel. The gradient magnitude (G) and the intensity gradient (Φ) were computed with the following equations:

$$G = \left(G_x^2 + G_y^2\right)^{1/2} \quad (5)$$

$$\Phi = \tan^{-1}(G_x/G_y) \quad (6)$$

The orientation for each 2 pixel × 2 pixel sized sub-region was evaluated over the entire image. For the deflection AFM images, cellular and background areas differed from image to image. To remove possible confounding effects, noisy sub-regions were excluded from the gradient evaluation if both the mean and variance (ANOVA) fell below threshold values determined from analysis of background areas of the deflection images. The orientation of the sub-regions were computed using the value of the gradient magnitudes and orientation in the sub-regions pixel by pixel with eqn (7) (Karlon *et al.* 1999):

$$A^S(\theta) = \sum_{i,j} G(i,j) \frac{e^{2[\cos(z(\theta-\varphi_{ij}))]}}{e^2} \quad (7)$$

where θ was the 180th element including natural numbers from 1 to 180 with a step size of 1, representing the possible orientation value of the sub-regions. φ was the local pixel orientation and it was perpendicular to the Φ. A^S is the accumulator bin value of the sub-region, and the dominant orientation of the sub-region was determined by the maximal value of the A^S.

For the dominant stress fibre density evaluation, we first subtracted background noise from the AFM height image along the AFM probe scanning lines and converted it into a black–white binary image. The black–white height images were then subdivided into 2 pixel × 2 pixel sized sub-regions corresponding to the sub-regions at the same position (coordinates) in the deflection images. In order to only evaluate the alteration in density of the predominant actin stress fibres, we computed only the area fraction (defined as the ratio of the area covered by the observed stress fibres in the analysed area of the cell surface to the area devoid of stress fibres) of the actin stress fibres whose orientation angles were within ±10 deg around the dominant stress fibre orientation angle.

Western blotting on G-actin and F-actin

The relative amount of G-actin and F-actin was measured using an assay kit (BK307) from Cytoskeleton (Denver, CO, USA) as previously described (Staiculescu *et al.* 2013) with minor modifications. Freshly isolated VSMCs were

cultured in 35 mm dishes and pharmacologically treated as described above. Cells were lysed and homogenized in 100 μl of F-actin stabilization buffer and lysis buffer (LAS2). The cell lysates were centrifuged at 100,000 *g* for 60 min at 25°C to separate the G-actin (supernatant) and F-actin (pellet). The pellets were suspended in 100 μl cold F-actin depolymerization buffer and incubated on ice for 1 h with mixing every 15 min. Equal amounts of G-actin and F-actin were loaded and subjected to immunoblot analysis using an anti-α-actin antibody (clone 1A4, Sigma A2547). Chemiluminescence signals were detected by Bio-Rad Chemi-DOC XRS+ digital system and band intensities were quantified using ImageLab software (Bio-Rad, Hercules, CA, USA). In this study, the actin filament depolymerizing agent latrunculin A (LAT-A) and actin polymerizing agent jasplakinolide (JSP) were used as negative and positive controls, respectively.

Transfection with a green fluorescent protein (GFP)-tagged F–actin vector and confocal imaging

Primary VSMCs were cultured to grow until 80% confluent on 60 mm plastic tissue culture dishes and transfected with a GFP-tagged F-actin vector (p^{CAG}LifeAct-TagGFP2, Ibidi, Munich, Germany). The electroporation procedure was performed using a Lonza 4D Nucleofector (Lonza, Basel, Switzerland) with P1 solution (Lonza) and FF-130 programme following the protocol provided by Lonza. Transfected cells were maintained under culture conditions for 2–3 days and serum-starved overnight before visualizing on a confocal microscope (Fluoview 1000 confocal microscope system, Olympus Inc.) using an excitation wavelength of 488 nm. A through-focus image set was collected for each cell with a *z*-step interval of 0.2 μm.

Confocal image processing

Cell image segmentation, fibre orientation, and cell surface intensity analyses were carried out using a custom automated image analysis program written in MATLAB. The major steps of this analysis are described below.

Cell segmentation. Image stacks, (I(*x*,*y*,*z*)), consisted of a series of 2-D digital images collected at 0.2 μm depths in the *z*-axis. An initial histogram stretching step was used to remove outlier image intensity values and to enhance image contrast in this 3-D data set. An intensity histogram of the 3-D data was computed and 1% of voxels at the low and high ends of the histogram were eliminated, and the remaining values were linearly stretched. A 3-D binary intensity mask $\mathrm{Mask_I}(x,y,z)$ was generated by applying the Otsu threshold (Otsu, 1979) to the individual *Z*-stack slices of the enhanced 3-D data set. Spurious detections were filtered using a 3-D neighbour count. The 3-D binary mask was integrated in the *z* dimension to produce an initial 2-D cell mask. The 2-D cell mask was then refined using geodesic active contours (Ersoy *et al.* 2008; Hong *et al.* 2013) by initializing active contours from the convex hull of the initial 2-D mask and evolving them towards the outer boundaries of the cell.

Fibre detection and analysis. Linear structures in the images corresponding to fibres were detected by convolving each *Z*-stack slice by a series of oriented elongated Laplacian of Gaussian (eLoG) filters similar to that described by Zemel (Zemel *et al.* 2010). The algorithm uses *n* anisotropic Gaussians as shown in eqn (8):

$$G(x, y, \sigma_x, \sigma_y) = \frac{1}{2\pi\sigma_x\sigma_y} e^{-\left(\frac{x^2}{2\sigma_x} + \frac{y^2}{2\sigma_y}\right)} \quad (8)$$

Each Gaussian filter was rotated in steps of π/n from 0 to $\pi - \pi/n$, ($n = 15$ for this study). The Gaussian kernels were then convolved with the Laplacian filter to yield *n* eLoG kernels as shown below.

$$\mathrm{eLoG}(x, y) = \begin{bmatrix} 0 & -1 & 0 \\ -1 & 4 & -1 \\ 0 & -1 & 0 \end{bmatrix} G(x, y, \sigma_x, \sigma_y) \quad (9)$$

Local orientation was estimated as the orientation of the filter at the maximum response. In order to accommodate both thin and thick fibres, two sets of eLoG filters with the same major-axis variance, but differing minor-axis variances were applied. The filter with the highest response was considered to determine local linearity/fibre response and orientation. For each *Z*-stack slice eLoG filter responses were further filtered with the Otsu threshold and a 3-D binary fibre map $\mathrm{Mask_{F1}}(x,y,z)$ was obtained:

$$\mathrm{Mask_{F1}}(x, y, z) = \begin{cases} 1 & \mathrm{eLoG}(I(x, y, z)) > T_{\mathrm{Otsu}}(z) \\ 0 & otherwise \end{cases} \quad (10)$$

Oriented filters allow inference of curvilinear structures from punctuated noisy data. In order to reduce this blending effect, 3-D binary fibre map $\mathrm{Mask_{F1}}(x,y,z)$ was fused with 3-D binary intensity map $\mathrm{Mask_I}(x,y,z)$ resulted in $\mathrm{Mask_{F2}}(x,y,z)$ that includes only the voxels with both high intensity and strong fibre response:

$$\mathrm{Mask_{F2}}(x, y, z) = \mathrm{Mask_I}(x, y, z) \Lambda \mathrm{Mask_{F1}}(x, y, z) \quad (11)$$

Fibre orientations were analysed by constructing orientation histograms of pixels with a high intensity and strong fibre response (Mardia & Jupp, 2000).

Cell surface analysis. In order to visualize and analyse surface fibres, a surface height map was constructed by locating the top-most voxel height in $\mathrm{Mask}_{F2}(x,y,z)$ for each surface position (x,y).

$$\mathrm{Surface\_Height}\,(x,\,y) = \max\{z|\mathrm{Mask}_{F2}\,(x,\,y,\,z) = 1\} \tag{12}$$

Statistical analysis

All data are reported as the mean ± SEM. Statistically significant differences between the oscillation patterns in elasticity and adhesion force for pre-drug and post-drug periods were analysed with a paired sample *t* test. Statistically significant differences between the vehicle control and drug-treated experiments were analysed with a two-sample *t* test. A value of $P < 0.05$ was considered significant. Statistically significant differences between dominant actin fraction for pre-drug and post-drug periods were analysed with a two-sample *t* test. A value of $P < 0.05$ was considered significant.

Results

Alterations in the oscillatory patterns of VSMC elasticity following stimulation with vasoactive agonists

Figure 1 demonstrates that 20 min of treatment with agonists significantly altered the dynamic characteristics of the temporal behaviour. This was apparent in the oscillating pattern that was reflected in VSMC cortical elasticity recordings. The amplitude of oscillations in VSMC *E*-modulus was increased by treatment with ANG II compared to the pre-drug period (Fig. 1*A* *vs.* *B*). By comparison, ADO decreased the amplitude of oscillations (Fig. 1*C*). A vehicle control experiment showed no effect on the amplitude of oscillation in VSMC *E*-modulus (data not shown). An Eigen-decomposition of the VSMC *E*-modulus waveform revealed the three principal

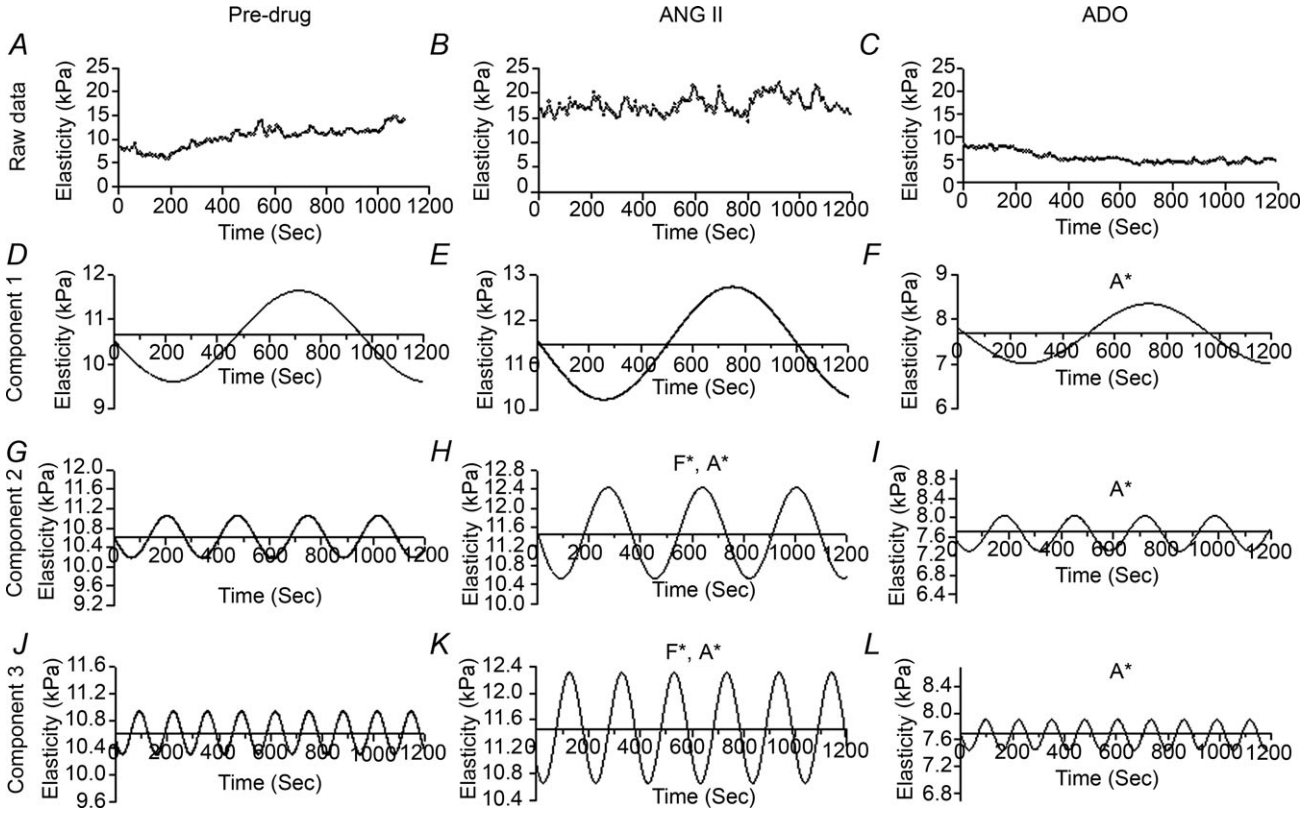

Figure 1. Eigen-decomposition of the VSMC *E*-modulus waveform used to identify three principal components of oscillation
The top panel illustrates the raw data for *E*-modulus during the pre-drug treatment period (*A*), post-ANG II treatment (*B*), and post-ADO treatment (*C*). ANG II treatment increased oscillation amplitude and ADO decreased the oscillation amplitude. Rows 2–4 illustrate the three oscillation components isolated using an Eigen-decomposition method: pre-drug period (*D*, *G* and *J*), 20 min post-ANG II treatment (*E*, *H* and *K*), and 20 min post-ADO treatment (*F*, *I* and *L*). F* and A* indicate that the frequency and amplitude of the component were significantly different from pre-drug period or vehicle control experiment, $P < 0.05$.

components in the oscillation pattern. Figure 1*D*–*L* illustrates the three components of the oscillation. In comparison with the pre-drug period (Fig. 1*G* and *J*), the ANG II treatment (Fig. 1*H* and *K*) significantly increased the amplitude of oscillation while reducing the frequency of oscillation for the second and third components ($P < 0.05$). In contrast, ADO (Fig. 1*F*, *I* and *L*) significantly decreased the amplitude of oscillation for all three components ($P < 0.05$).

Figure 2 displays the comparisons of the oscillation in adhesion force between the pre-drug period (Fig. 2*A*) and 20 min after treatment with either ANG II (Fig. 2*B*) or ADO (Fig. 2*C*). Using the Eigen-decomposition method we similarly isolated three principal components from the raw adhesion force data with respect to time. Compared with the pre-drug period (Fig. 2*D*, *G* and *J*), ANG II treatment increased the amplitude of oscillation of each component (Fig. 2*E*, *H* and *K*, $P > 0.05$), while ADO (Fig. 2*F*, *I* and *L*) had no significant effect.

In order to understand whether there was a potential mechanistic link between the oscillation in *E*-modulus and cell adhesion, we compared the oscillation periods for the three components of *E*-modulus and adhesion as shown in Fig. 3. The oscillation period for component 1 of adhesion is in the same range as component 2 of the *E*-modulus and these components are indicated as group I. These two components showed almost the same mean value at approximately 300 s. Component 2 of the adhesion force and component 3 of the *E*-modulus were also in the same range of oscillation period between 50 and 250 s and are indicated as group II.

Cytoskeleton remodelling occurs during stimulation with vasoactive agonists

In this study, the detailed temporal analysis of changes in VSMC *E*-modulus and adhesion was conducted using an Eigen-decomposition method and the oscillations in these variables compared with changes in cytoskeletal remodelling. We hypothesized that the oscillations and cytoskeletal remodelling were linked processes. In our previous study, real time measurement on cell elasticity revealed that vasoactive agonists immediately induced changes in the cell *E*-modulus and adhesion that took 15–20 min to reach an equilibrium state after drug

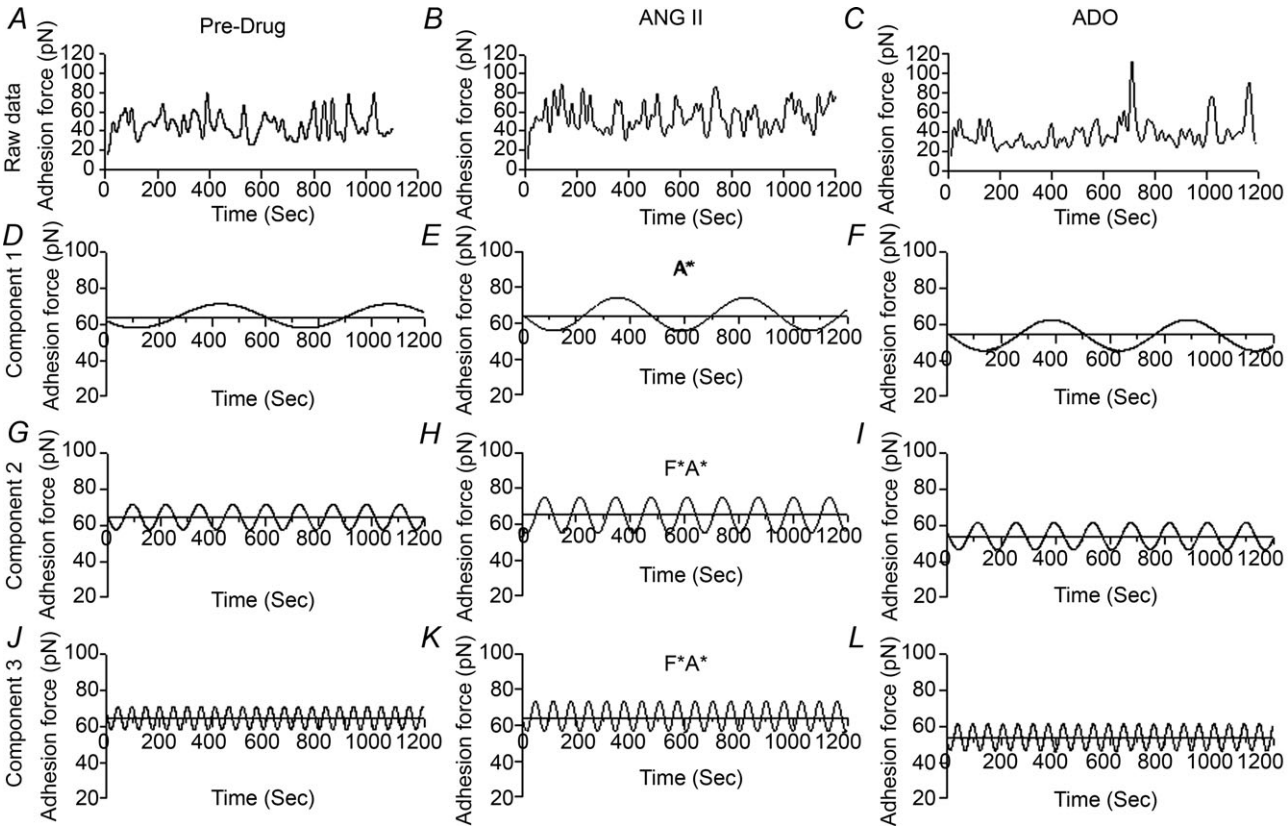

Figure 2. Oscillation pattern of the adhesion force of VSMCs treated with different vasoactive agonists
The top panel displays the time series of raw adhesion data for pre-drug period (*A*), post-ANG II treatment (*B*), and post-ADO treatment (*C*). ANG II treatment increased the oscillation amplitude and ADO decreased the oscillation amplitude. Rows 2–4 illustrate the three components isolated using an Eigen-decomposition method: pre-drug period (*D*, *G* and *J*), 20 min post-ANG II treatment (*E*, *H* and *K*), and 20 min post-ADO treatment (*F*, *I* and *L*).

stimulation (Hong *et al.* 2012). Additionally, effects of these agonists on oscillation were evident within seconds and changes in oscillation could be visibly observed (Hong *et al.* 2012). In order to perform a more detailed analysis of the agonist-induced changes in oscillation and cytoskeletal architecture, we chose for technical and practical reasons to analyse the oscillation behaviour at 20 min after agonist treatment when the *E*-modulus appeared to reach equilibrium. Our current interpretation is that the oscillations are sensitive to the state of the cytoskeleton and influenced by cytoskeletal remodelling thus linking the two processes. Clearly, even after significant cytoskeletal remodelling had occurred the oscillations continued and did not return to control values suggesting that they reflected a new cytoskeletal state.

Architectural changes in the submembranous cortical cytoskeletal structure (100–300 nm depth) were assessed by imaging of the VSMC topography followed by quantification of alterations in stress fibre density and orientation. Figure 4 displays the contact mode height images of typical VSMCs for pre- and post-drug treatment. Height image acquisition was performed at 0.4 Hz (approx. 25 min per image at 512 pixels × 512 pixels). The blue squares in the upper left panels of Fig. 4*A*–*D* indicate the areas of the cell surface that were scanned by AFM probe to obtain the height signals (post-drug scan initiated at 20 min after treatment). The upper right panel of Fig. 4*A* shows the pre-drug cell height image (40 μm × 40 μm). The cross-section of cell surface, obtained along the red line in the height image for the pre-ANG II treatment period, is shown in the lower panel of Fig. 4*A*. Figure 4*B* shows the height image and cross-section of the VSMC (same cell as in Fig. 4*A*) following 20 min of ANG II treatment. In comparison with the pre-drug period (Fig. 4*A*), treatment with ANG II resulted in an increase in stress fibre density and height (Fig. 4*B*). In response to ADO the results showed an opposite effect with regard to the stress fibre density and height. Treatment with ANG II and ADO also appeared to significantly affect fibre orientation and thickness. For example, ANG II appeared to increase orientation and thickness, similar to what would be expected with activation of polymerization, and treatment with ADO appeared to decrease orientation and fibre thickness, consistent with a process of depolymerization of the stress fibres (right panel of Fig. 4*D*), and also decreased stress fibre height compared to the pre-ADO treatment period (Fig. 4*C*). Vehicle control experiments, using buffer alone, showed no significant difference in the measurement for the pre-buffer and post-buffer periods (Supporting information Fig. S3).

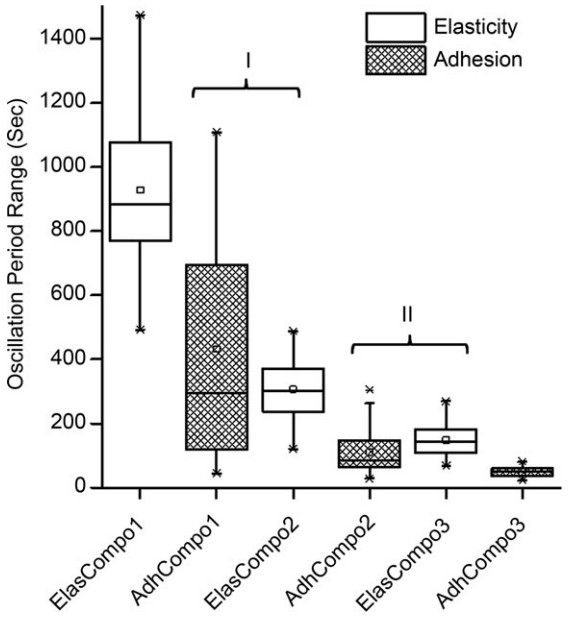

Figure 3. Comparison of oscillation periods for the three components of *E*-modulus and cell adhesion
Oscillation periods are summarized for the various oscillation components. The oscillation period for component 1 of adhesion had the same mean value as component 2 of the *E*-modulus, indicated as group I, and component 2 of adhesion and component 3 of the *E*-modulus are in the same oscillation period, indicated as group II.

To more accurately quantify changes in fibre orientation we performed an orientation analysis on the fibres present in the topographic images. Figure 5 displays a single cell example of the quantification approach used to detect the alterations in actin stress fibre orientation and density for pre- and post-ANG II treatment. The deflection and height signals were recorded simultaneously in each sample in contact mode. The deflection image was subdivided into 250 × 250 sub-regions, with each sub-region being 2 pixels × 2 pixels in size. The actin stress fibre orientation and density of each sub-region was analysed with a custom developed MATLAB image-processing method. Figure 5*A* shows a raw deflection image for the pre-ANG II treatment period. Figure 5*B* provides a pseudo-colour map for the orientation of each 2 × 2 pixel sub-region of the entire deflection image. The different colours represent different orientations of actin stress fibres in each sub-region from +90 deg to –89 deg with 0 deg arbitrarily selected as the major fibre orientation in order to provide a means for normalizing cell-to-cell differences in orientation. Figure 5*C* is a histogram plot of total actin stress fibre orientation in sub-regions over the entire deflection image during the pre-ANG II treatment period. Again, in order to statistically analyse the deflection images from a group of cells and normalize images with respect to each other and summarize orientation data, the dominant direction over the entire image was arbitrarily considered as 0 deg. Based on the 0 deg normalization, the directions of 2 × 2 pixel sub-regions in the histogram were then normalized to the angle of fibres relative to this dominant direction. Figure 5*D* shows a black and white image converted from the cell height image to correspond

to the dominant actin stress fibre in deflection image (from Fig. 5*A*). The white area represents the sub-regions in which the fibre orientation was within the range of ±10 deg of the major orientation direction. Panels *E–H* provide the corresponding images for the 20 min post-ANG II treatment period. All images were obtained using the same criteria as described for image acquisition and processing prior to ANG II treatment. The results demonstrate that under these conditions ANG II significantly enhances the alignment of stress fibres and increases the dominant actin area fraction by 35%.

Figure 6 shows an example of the alterations in actin stress fibre orientation and density for pre- and post-ADO treatment. Panels *A–D* represent the pre-ADO treatment period and panels *E–H* represent the images at 20 min post-ADO treatment. All images in Fig. 6 were obtained using the same criteria as described for the corresponding panels in Fig. 5. The results showed that ADO significantly

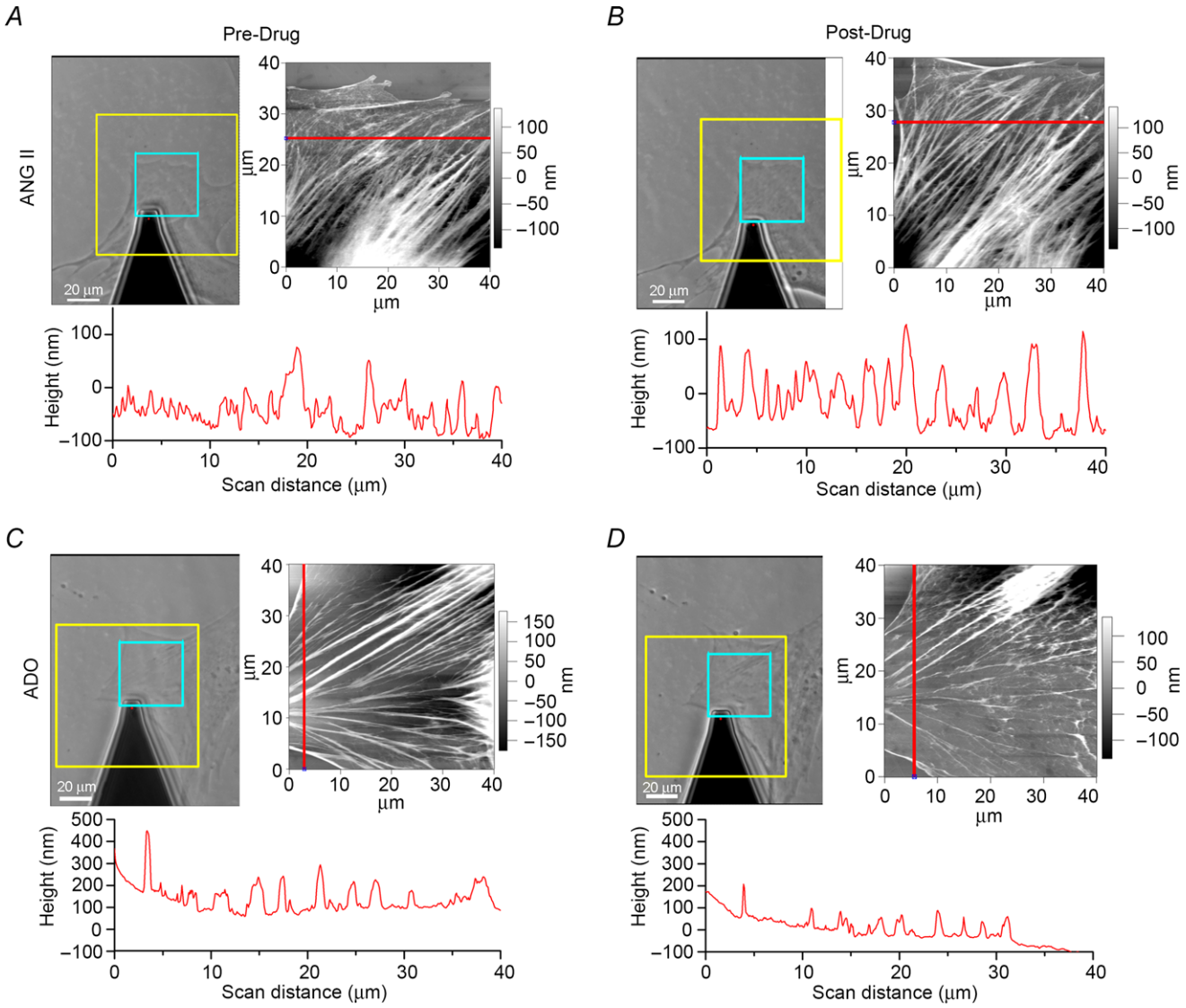

Figure 4. Cell height image acquired with AFM in contact mode
A and *B* display the cell height image for pre- and 20 min post-ANG II treatment period, respectively. *C* and *D* show the cell height image for pre- and 20 min post-ADO treatment period, respectively. The upper left panel for each group of panels illustrates the phase contrast image for the cell that was subjected to AFM probe scanning, in which the yellow square shows the maximal accessible area for the AFM probe and the blue square shows the area that was experimentally scanned for the height image acquisition. The upper right panel of each group was the cell height image (40 μm × 40 μm). Acquisition of the height image was conducted at 0.4 Hz frequency and it took approximately 25 min to obtain a cell topography image with 512 × 512 pixels in digital size. The red line in the lower panel in each group is a height cross-section of the cell surface along the line indicated for the corresponding height images of each group.

decreased both the alignment of stress fibres and the dominant actin density. These data quantitatively support and were consistent with the stress fibre morphology presented in Fig. 4.

As a control, we also assessed the effect of the vehicle buffer on actin stress fibre orientation and density for pre- and post-vehicle addition to the cell bath. The vehicle control experiments did not demonstrate any significant difference in stress fibre orientation or actin density between pre- and post-buffer period (Supporting information Fig. S4).

Alterations in the distribution of the actin stress fibre orientation were grouped for all the cells studied to show changes in density of dominant stress fibre following treatment with vasoactive agonists (Fig. 7). The upper panels display the summaries of the stress fibre orientations plotted as histograms of fibre angle distribution over entire deflection images. The grouped results (Fig. 7*A*) showed that ANG II enhanced the alignment of actin stress fibres, while ADO treatment led to a more heterogeneous distribution pattern, spreading the distribution of the stress fibres (Fig. 7*B*). Time control experiments showed that administration of vehicle did not significantly change the orientation of stress fibres (Fig. 7*C*). The lower panels display the summarized group data for the dominant actin stress fibre area fraction in the sub-regions of the height images, in which the pixel orientations were in the range of ± 10 deg of the dominant stress fibre direction over the entire deflection image. As shown in Fig. 7*D*, ANG II significantly increased the actin density in the dominant sub-regions ($n = 7$, $^*P < 0.01$), while ADO treatment significantly decreased dominant actin stress fibre density (Fig. 7*E*, $n = 9$, $^*P < 0.01$). Time control experiments showed no difference in actin density between the pre- and post-buffer periods (Fig. 7*F*).

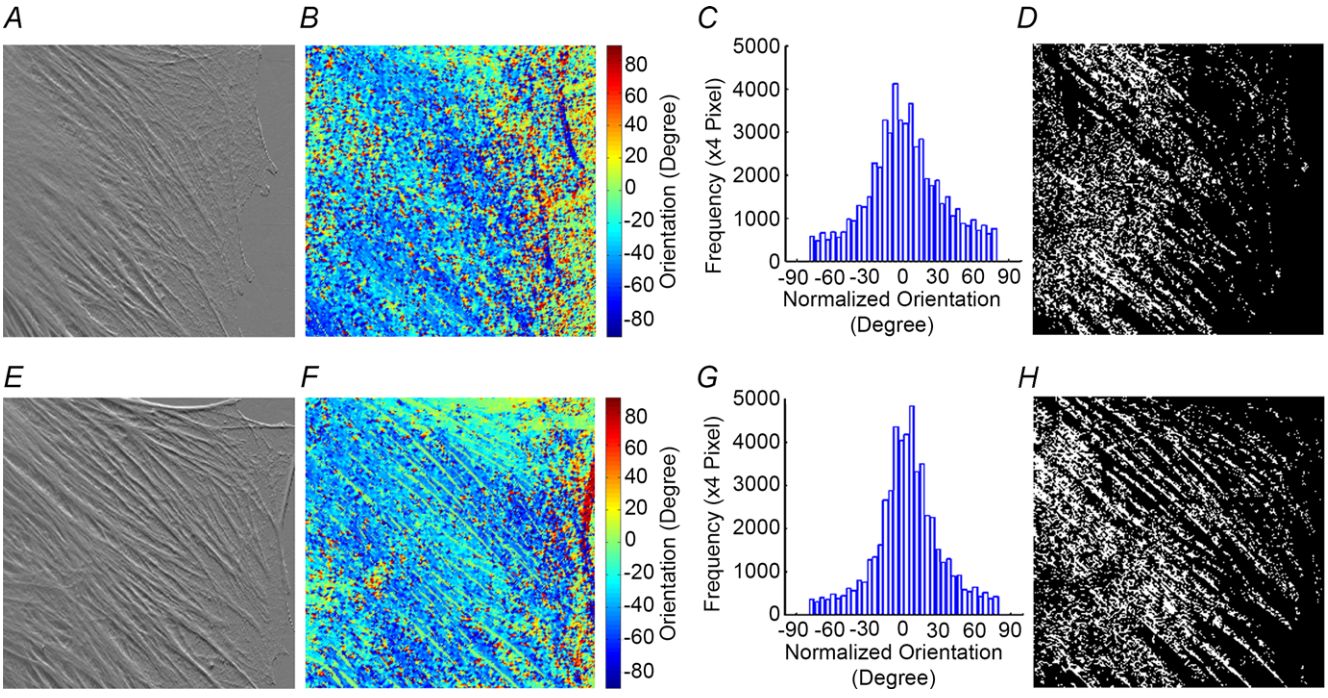

Figure 5. A representative alteration in actin stress fibre orientation and density for pre- and post-ANG II treatment

Acquisition of the deflection image was conducted at 0.4 Hz. The deflection signal and height signal were recorded simultaneously at the same individual scanning in contact mode. The deflection image was subdivided into 250 × 250 sub-regions, and each sub-region was 2 pixels × 2 pixels in size. The actin stress fibre orientation and density of each sub-region was analysed with a MATLAB image processing methodology developed in this study. *A*, raw deflection image for the pre-ANG II treatment period. *B*, pseudo-colour map for the orientation of each sub-region in the entire deflection image. The different colours represent the different directions/angles of actin stress fibre in the sub-regions. *C*, histogram of total actin stress fibre orientation in sub-regions over entire deflection image for the pre-ANG II treatment period. The orientation of each sub-region is the normalized angle of fibre direction. The dominant direction over the entire image was arbitrarily considered as 0 deg. *D*, black–white image for the dominant orientation of the stress fibre. The white area stands for the dominant sub-region, in which the fibre orientation was in the range of ± 10 deg. *E*, *F*, *G* and *H* represent the images for the 20 min post-ANG II treatment period and all images were obtained by the same criteria as described for the corresponding panels in the pre-ANG II treatment period.

Western blotting experiment for the measurement of G/F ratios following ANG II or ADO in VSMCs

To examine whether ADO and ANG II have effects on actin polymerization, we measured changes in the ratio of G-actin to F-actin in whole VSMCs. LAT-A and JSP, agents known to prevent actin polymerization and to stabilize F-actin, respectively, were used as controls. Figure 8*A* and *B* shows that LAT-A significantly increased the amount of G-actin and JSP increased the amount of F-actin in VSMCs as predicted. No statistically significant change in whole VSMC G/F actin ratio was detected in response to ANG II treatment ($n = 5$, $P > 0.05$). However, ADO significantly increased the G/F actin ratio by approximately 58% ($n = 5$, $P < 0.05$), consistent with the AFM topology analysis.

Confocal image analysis of GFP-tagged F-actin distribution following treatment with vasoactive agonists

Confocal images for the GFP-tagged endogenous F-actin in VSMCs before and after treatment with various vasoactive agonists are displayed in Fig. 9. Primary VSMCs were grown in culture until 80% confluent on 60 mm plastic tissue culture dishes and transfected by electroporation with a GFP-tagged F-actin labelling vector. Labelled cells were cultured for 2–3 days and serum starved overnight before performing confocal microscopy. Figure 9*A* and *B* shows the representative confocal images of actin stress fibres prior to ANG II treatment and 30 min post ANG II treatment, respectively. Images represent the through-focus distribution of actin for the whole VSMC. Figure 9*E* and *F* presents the representative confocal images of actin stress fibres prior to and 30 min following ADO treatment, respectively.

To detect the orientation of actin stress fibres the fluorescent confocal images were analysed using a similar method to that described previously (Zemel *et al.* 2010). The 1–180 deg of orientation angles of the stress fibres was subdivided into 15 equal orientation angles with a step size of 12 deg. To visualize the orientation of the actin stress fibre, the fibre maps were plotted with 15 pseudo-colours, where each different colour represented a different orientation angle of the actin stress fibres (Fig. 9*C*, *D*, *G* and *H*). The results demonstrated that ANG II stimulation did not significantly increase the stress fibre thickness and alignment in comparison with the pre-ANG II condition when the thickness and distribution of actin fibres through the whole cell were analysed. These results were consistent with the Western blotting showing no change in the G/F ratio, but they contrasted with the change in cortical actin behaviour revealed by the AFM topology imaging. In contrast, 30 min after ADO treatment, confocal images of actin stress fibre

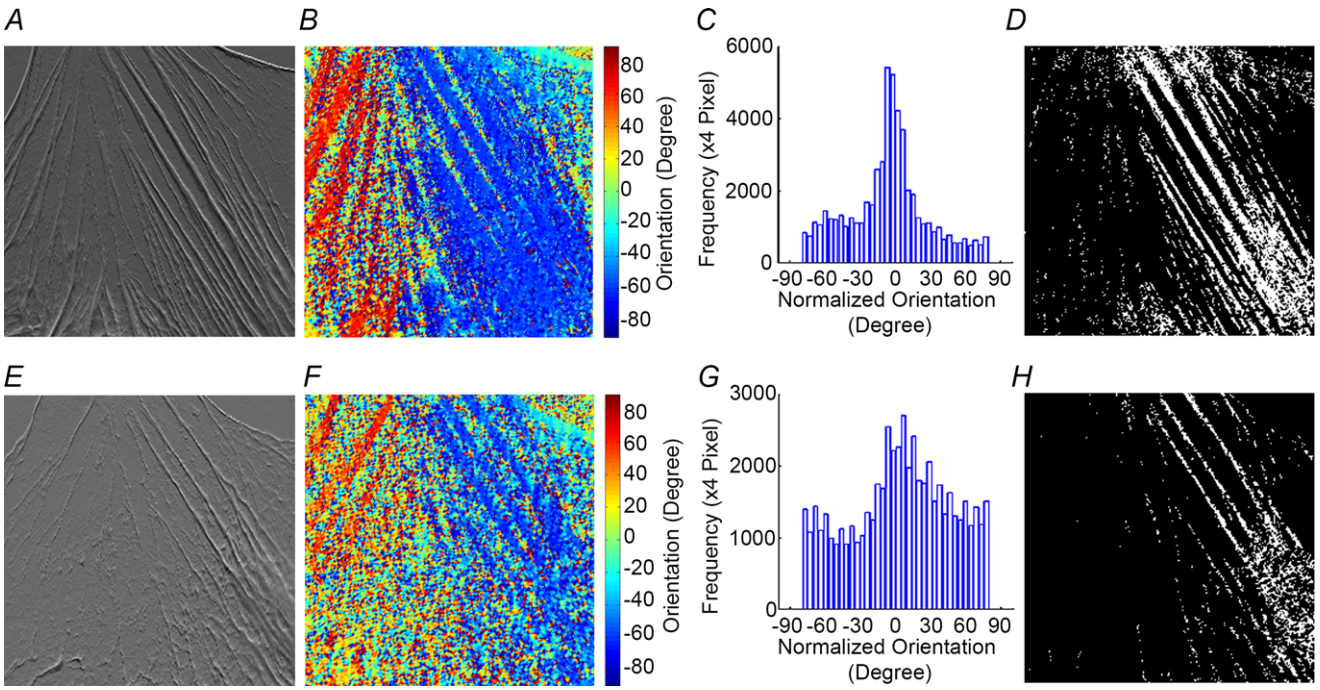

Figure 6. A representative alteration in actin stress fibre orientation and density for pre- and post-ADO treatment
A, *B*, *C* and *D* represent the images for the pre-ADO treatment period. *E*, *F*, *G* and *H* display the images for the 20 min post-ADO treatment period. All of the images were obtained by the same criteria as described for the corresponding panels in the ANG II experiment (Fig. 5).

distribution showed a drastically dissembled morphology and reoriented network of filaments in comparison with the pre-ADO period. These results were consistent with depolymerization indicated by Western blotting and revealed by AFM topology imaging.

In order to further test the effect of vasoactive agonists on the architecture of submembranous actin stress fibres, the surface actin structure was analysed by detecting the top 200 nm of fluorescence signal from confocal *Z*-stacks using a custom designed MATLAB image-processing method. The result is a 2-D display (Fig. 10*A*) of the entire 3-D cell surface that maps the actin within the near-surface volume. The colours represent height of the fluorescence signal. Figure 10*A* and *B* shows the height image of the surface fluorescence signal for the control cell and 30 min after ANG II treatment. These images were obtained by analysis of the raw confocal images without filtering. Figure 10*C* and *D* presents the height images of the surface actin stress fibre for the control cell and 30 min after ANG II treatment. These images were obtained by analysing confocal images after filtering to enhance and detect fibrous structures. Figure 10*E–H* shows the height images before and after ADO treatment. These images were obtained with the same method as ANG II treatment. Figure 10 clearly demonstrates that ANG II mostly affects the architecture of a compartment of submembranous actin stress fibre, whereas ADO leads to actin fibre disassembly within the whole cell. For ANG II treatment these confocal data were consistent with the AFM topology data but not the Western blot

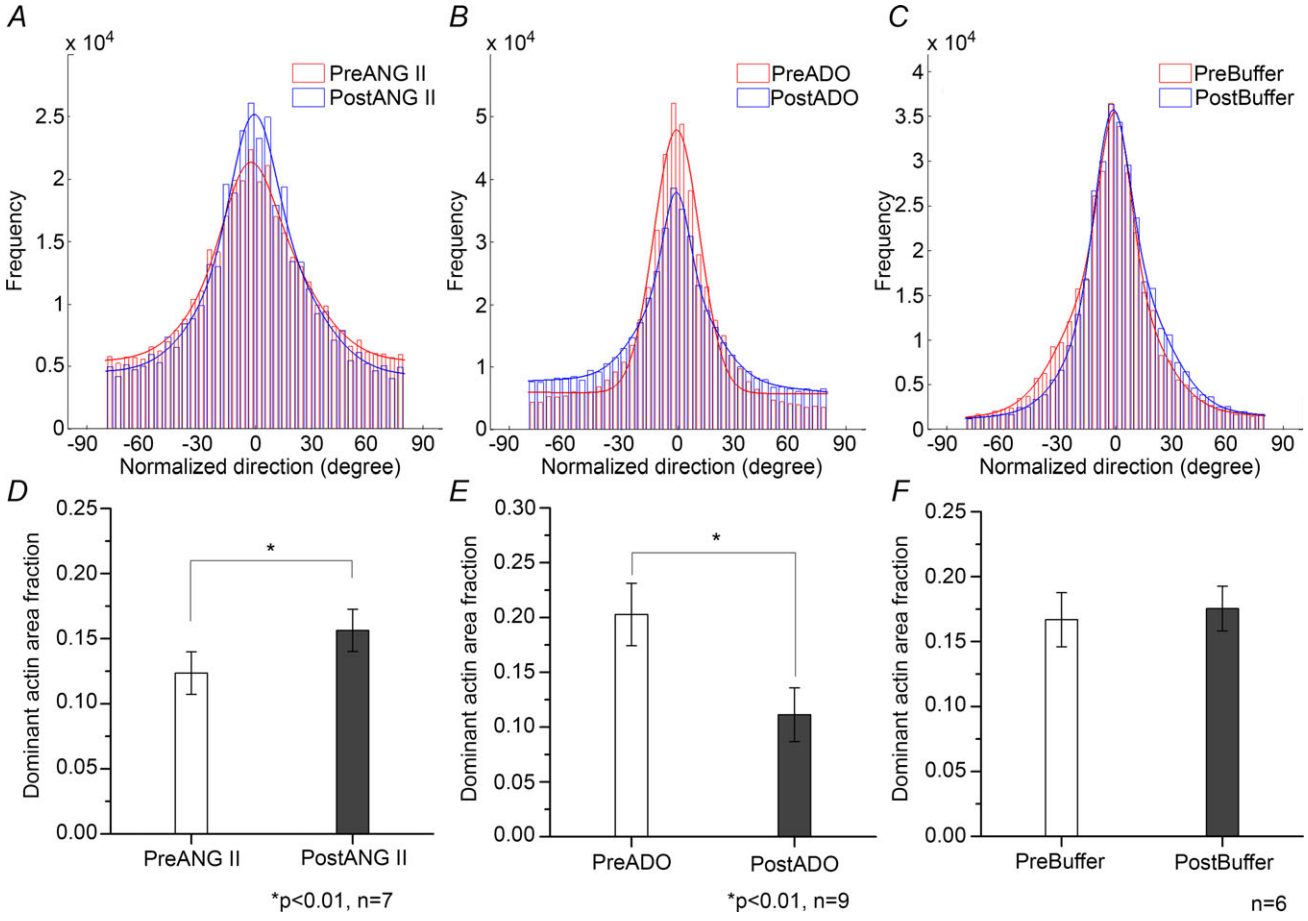

Figure 7. The alteration in the distribution of the actin stress fibre directions for the entire deflection image and in the stress fibre area fraction following treatment with vasoactive agonists
A, histogram of the orientation distribution for the pre-ANG II treatment period and post-ANG II treatment. *B*, histogram of the orientation distribution for the pre-ADO treatment period and post-ADO treatment. *C*, histogram of the orientation distribution for the pre-vehicle treatment period and post-vehicle treatment. *D*, the actin stress fibre area fraction of the sub-regions in height images between the pre- and post-ANG II treatment ($n = 7$, $^*P < 0.01$). *E*, the actin stress fibre area fraction of the sub-regions in height images between the pre- and post-ADO treatment ($n = 9$, $^*P < 0.01$). *F*, the actin stress fibre area fraction of the sub-regions in height images between the pre- and post-vehicle buffer treatment ($n = 6$, $^*P > 0.05$). These three bar graphs only summarize the sub-regions of the height images in which the pixel orientations were within the range of ±10 deg in the deflection image.

data representing whole cell actin. For the ADO treatment these confocal data are consistent with the Western blot data, the whole cell fluorescent actin data and the AFM topology data.

Discussion

Previously we have shown in VSMCs that vasoactive agonists induce coordinated changes in elasticity and integrin-mediated cell adhesion. Thus, vasoconstrictors increase VSMC *E*-modulus and simultaneously enhance cell adhesion, whereas vasodilators have the opposite effect (Hong *et al.* 2012). In this study, extension of these studies into the time domain has revealed that the changes in elasticity are underlain by active spontaneous oscillations in cell elasticity and adhesion. Furthermore, these oscillation patterns were altered by the vasoactive agonists. These oscillations strongly support the operation of very dynamic intracellular processes and further support evidence that the outside-in signalling pathways driven by ANG II and ADO are linked to both the cytoskeleton and cell adhesion. Spontaneous oscillations in cell elasticity have been reported for multiple cell types (Schillers *et al.* 2010; Végh *et al.* 2011; Zhu *et al.* 2012); some of the available evidence to date suggests they are perhaps linked to myosin motors and myosin light chain kinase activity (Schillers *et al.* 2010).

Despite some minor advances in understanding the signalling pathways that alter the oscillations, the exact mechanisms and the biological functions of these oscillations in cell elasticity and adhesion remain unclear (Kruse & Jülicher, 2005). This, therefore, requires further exploration at the single cell and intact tissue levels to resolve their functional implications. The physiological role of these oscillations in VSMCs is as yet unidentified but we can speculate upon several functional possibilities. First, viewed from the isolated single cell scale these oscillations may reflect the underlying dynamic properties of the biochemical signalling that reflect the state of the cytoskeleton and that drive cytoskeletal and adhesive behaviour. Second, from a functional point of view these oscillations may reflect a mechano-sensing cellular behaviour, allowing sampling of the surrounding mechanical and chemical environment. This sampling could also include the cell searching for specific extracellular matrix (ECM) binding sites or other cell types. Third, if this oscillation behaviour is considered in the context of an intact arterial wall, it is possible that the mechanism involves communicating mechanically with neighbouring VSMCs or with other vascular wall cell types such as endothelial cells. If communication with neighbouring cells is important, then our observation that the oscillations change on agonist stimulation is suggestive of a role in entraining and coordinating mechanical behaviour amongst groups of cells within the vascular wall, thus improving collective mechanical performance and cell-to-cell cooperation. Cells that strongly oscillate could act to drive performance of more-weakly oscillating neighbouring cells much like pacemakers within the vessel wall. Determining the mechanisms and functions of the oscillations should certainly prove an exciting avenue of future research.

In this study, one of the key questions we sought to answer was whether mechanisms underlying these oscillations were influenced by vasoactive agonists. To accomplish this in single VSMCs it was necessary to develop several novel experimental approaches and analysis routines. The VSMCs used in this study were freshly isolated and placed in culture without any passage to minimize the effect of the phenotypic change on the mechanical properties. Unfortunately, use of freshly isolated VSMCs (without culture) was not suitable for testing the mechanical properties due to technical limitation in our AFM approach. The cell *E*-modulus measurements in our study were conducted by repetitively nano-indenting (100–300 nm) into the cell surface with a spherical AFM probe, so that the cell *E*-modulus measured in this protocol primarily reflects the mechanical properties of the submembranous cytoskeleton (i.e. cortical region). In this

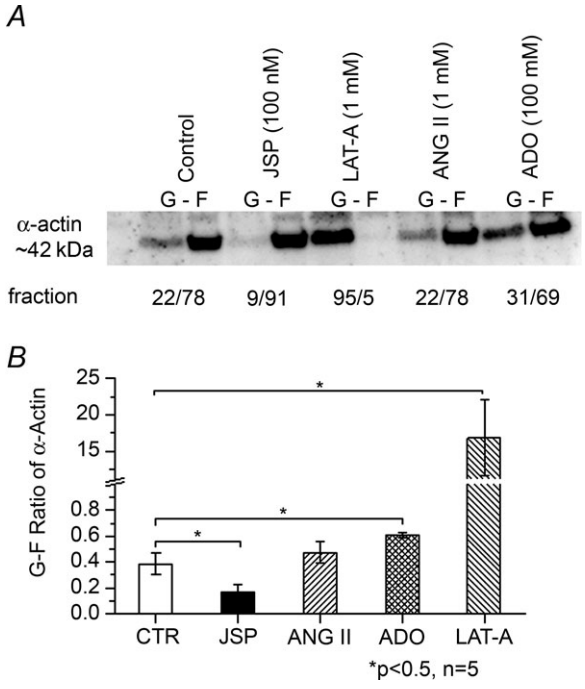

Figure 8. Western blotting confirmed that ADO treatment led to disassembly of F-actin in VSMCs
A, representative Western blot result. The G/F ratio of α-actin was increased by stimulation with ADO from 22/78 to 31/69 in this individual experiment. *B*, summarized group data showed the statistically increased G component in the actin cytoskeleton. $^*P < 0.05$, $n = 5$. LAT-A and JSP were used as negative and positive controls, respectively.

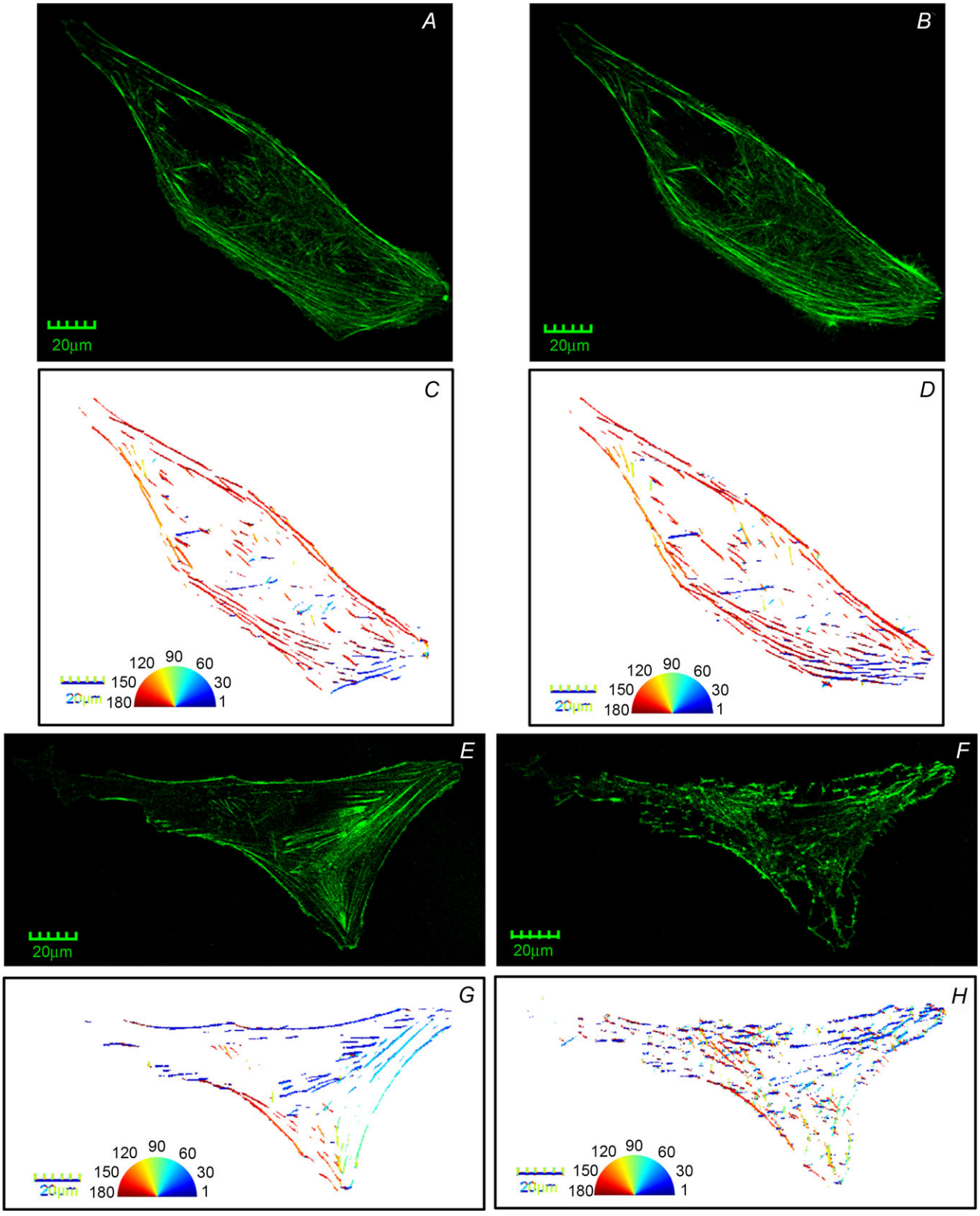

Figure 9. Confocal images for the GFP-tagged endogenous F-actin in VSMCs under the condition of treatment with various vasoactive agonists

case, we hypothesized that the oscillations in cell elasticity and adhesion were being driven by the sub-surface cortical cytoskeletal rearrangement and adhesive adaptations that could be modulated by vasoactive agonists. It is well established that the cortical cytoskeleton network physically connects to deeper cytoskeletal elements within the cytosol as well as to adhesion zones that regulate adhesion to the ECM. Furthermore, it is well recognized that the cytoskeletal network physically connects the intracellular compartment of the cell to extracellular matrix and adjacent cells and that it can dynamically rearrange its architecture in response to cell shape alterations, as well as cell movement in response to chemical and mechanical stimulation through the surrounding environment (Gunst & Zhang, 2008). Therefore, it is not surprising that the cytoskeleton would exhibit a highly dynamic behaviour probably reflecting the cell's ability to continuously adjust and adapt. This was apparent in the changes in oscillation patterns of cell elasticity following agonist treatment.

In addition to the dynamic temporal behaviour, live cells also show spatially dependent properties in their *E*-modulus, i.e. the confluent cells show a longer oscillation period in *E*-modulus than do sub-confluent cells (Végh *et al.* 2011). Furthermore, cells are typically softer over the nucleus than over cytoplasmic areas (Ruiz *et al.* 2012). Viewing the cytoskeleton and adhesion as dynamic properties, it is likely that the oscillations observed in cell elasticity and adhesion are a further reflection of the continually on-going adaptive behaviour to mechanical and chemical changes in their environment. These oscillatory changes might be important not only for cells in sensing changes in the extracellular environment and rapidly adapting but also for mechanical communication with neighbouring cells. Although, not directly studied in this investigation but pertinent in the context of the vascular wall, rapid changes in cell elasticity and adhesion may be coordinated with changes in force generation by the VSMCs or the extramural forces to which they are exposed.

In testing our hypothesis, we first analysed the time series of raw *E*-modulus data with an Eigen-decomposition method as described previously (Zhu *et al.* 2012). This mathematical (Eigen-decomposition) analysis enabled us to isolate oscillation components and their characteristic amplitude and frequency while eliminating noise from the oscillation pattern. In our study, three major components of oscillation were studied. ANG II drastically induced an increase in the amplitude of *E*-modulus oscillation and reduced oscillation frequency, while ADO was effective at attenuating the oscillation amplitude. These alterations in oscillation behaviour are hypothesized to be related to rapid changes in the properties of submembranous cortical actin cytoskeleton. The Eigen spectral analysis of the adhesion force data also demonstrated the presence of dynamic oscillatory behaviour in cell adhesion or stickiness to the ECM protein FN (Fig. 2). ANG II significantly induced increases in the amplitude while reducing the frequency of adhesion oscillation. However, ADO had no statistically significant effect on adhesion oscillation. It was noteworthy that the periods of the components 1 and 2 of the oscillations in cell adhesion were highly synchronized with the components 2 and 3 of the oscillation in cell *E*-modulus (Fig. 3), respectively. This observation suggests that these components of oscillation in cell *E*-modulus and adhesion may be dynamically linked by shared signalling pathways.

The period of spontaneous cellular Ca^{2+} oscillations is approximately 200 s (Tsien & Tsien, 1990; Kim *et al.* 2009; Imtiaz *et al.* 2010; Uhlén & Fritz, 2010), which is in the same range as that for component 1 of the adhesion and component 2 of the cell elasticity in the present study. These findings suggest that in VSMCs these synchronized oscillatory components in cell elasticity and adhesion could be related to the spontaneous Ca^{2+} oscillations. Further supporting this, our previous study demonstrated that a myosin motor was involved in dynamic oscillations in cell elasticity (Zhu *et al.* 2012), which was also consistent with the dynamic instability of the epithelial cell elasticity reported by Schillers *et al.* (2010). Schillers *et al.* also concluded that acto-myosin motor activity driven by Ca^{2+} oscillation was involved as a potential elasticity oscillator in their cell system.

In addition to the Ca^{2+}-dependent myosin motor mechanism, our AFM imaging results (Figs 5–7), Western blotting data (Fig. 8), and confocal images (Figs 9 and 10) clearly indicate that alterations in cytoskeleton architecture, resulting from assembly and/or disassembly of F-actin, also appear to play a significant role in the oscillatory behaviour of VSMC elasticity. The apparent

A, GFP-tagged F-actin before ANG II treatment. *B*, GFP-tagged F-actin 30 min after ANG II treatment. *C* and *D*, the fluorescent confocal images were analysed with MATLAB to detect the orientation of stress fibre for the pre- and post-ANG II treatment, respectively. The 1–180 deg of orientation angle of stress fibre was homogeneously subdivided into 15 orientation angles with a step of 12 deg. The different colours represent the different orientations of actin stress fibres. *E*, GFP-tagged F-actin before ADO treatment. *F*, GFP-tagged F-actin 30 min after ADO treatment. Confocal image demonstrates the slight changes in F-actin architecture induced by ANG II treatment and the depolymerization of actin stress fibre resulting from administration of ADO in the cell bath. *G* and *H*, the respective orientation plots, where the different colours represent the different orientation of actin stress fibres. Scale bars in *A*, *B*, *E* and *F* are 20 μm.

inability of Western blotting to detect changes in the G/F actin ratio following ANG II treatment may reflect differences in the methodology for quantification that are related to spatial differences in actin behaviour in different cellular compartments. Thus, it is important to consider that whole cell changes in the G/F actin ratio may not accurately reflect what is happening at the level of the submembranous cortical domain. Changes in this specific local domain may effectively be 'diluted' if only whole cell values are considered. Supporting this contention, confocal image analysis demonstrated that ANG II only induces changes in the orientation and thickness of submembranous actin stress fibres instead of globally affecting the cytoskeletal architecture as was evident for ADO (Figs 9 and 10). Intriguingly this raises the possibility that ANG II and ADO may affect the actin cytoskeletal architecture by differing, but perhaps overlapping, mechanisms. One possible pathway by which ADO causes disruption of actin stress fibre assembly is through a Ca^{2+}-independent Rho pathway as reported by Rex *et al.* (2009). In this mechanism, ADO-induced depolymerization of F-actin occurs by activating the F-actin cleavage protein cofilin via decreasing its phosphorylation state. The alignment of the submembranous cytoskeleton induced by ANG II may also be related to reorganization within the focal adhesion complex as reported recently (Poythress *et al.* 2013).

In summary, our results show that vasoactive agonists caused dynamic oscillatory changes in cell elasticity and adhesion that were accompanied by submembranous cytoskeleton remodelling. These alterations in elasticity and adhesion may play an important role in the normal VSMC response to agonists and reflect adjustments related to force generation and transmission between and within the VSMC as well as maintenance of vascular tone within the vascular wall. Additional studies will be required to verify these points and to identify the underlying biological signals that drive the oscillations and link elasticity and adhesion. As VSMC elasticity and adhesion are affected by ageing (Qiu *et al.* 2010) and hypertension (Sehgel *et al.* 2013), a deeper understanding of the underlying

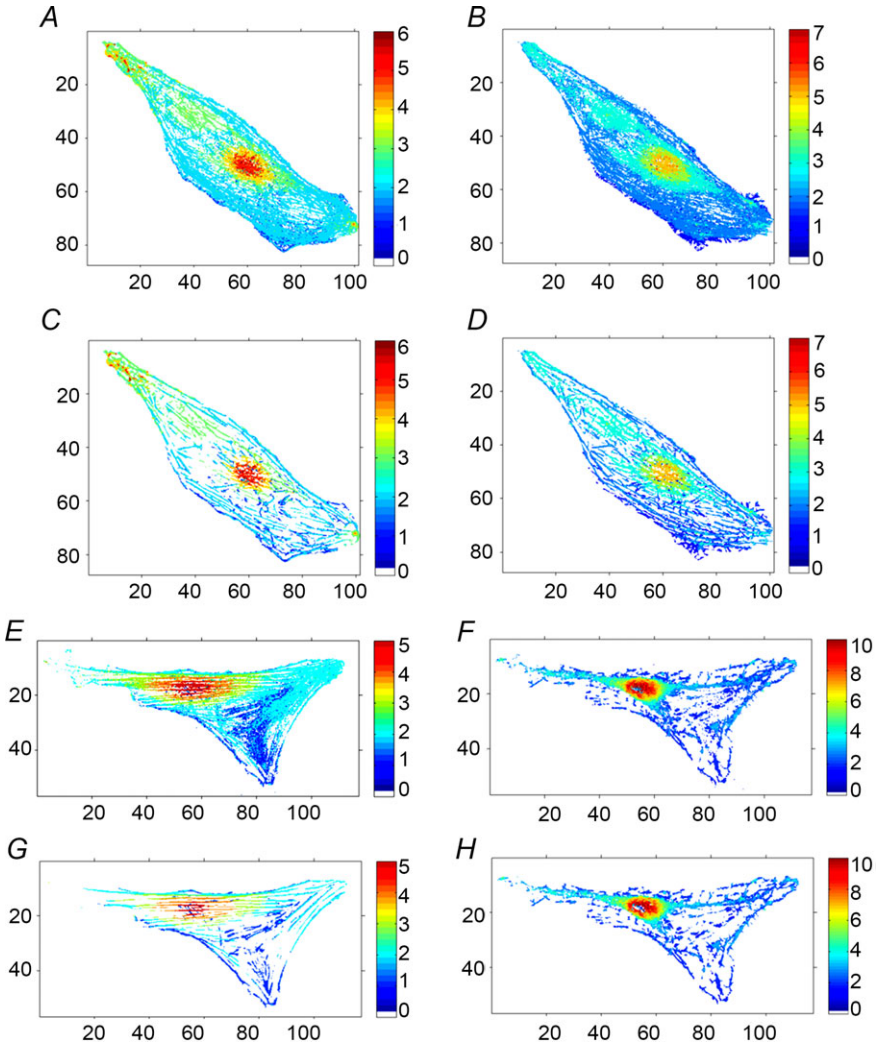

Figure 10. The effect of vasoactive agonists on the submembranous actin stress fibre architectures
The surface actin stress fibre structure was obtained by detecting the top 200 nm depth of fluorescence signal from confocal *Z*-stacks with a MATLAB image processing method. *A* and *B*, the height images of the surface fluorescence signal for a control cell and 30 min after ANG II treatment. These images were obtained by analysing the raw confocal images without fibre filtering (Fig. 9*A* and *B*). *C* and *D*, the height images of the surface actin stress fibres for a control cell and 30 min after ANG II treatment. These images were obtained by analysing the filtered confocal images for fibrous structure. *E* and *F*, the height images of the surface fluorescence signal for a control cell and 30 min after ADO treatment. *G* and *H*, the height image of the surface actin stress fibre for a control cell and 30 min after ADO treatment. The height values range from low (blue, green) to high (yellow, red). The axis unit is μm.

mechanism may also improve our understanding of how VSMC elasticity is regulated and certain vascular disease conditions as well.

References

Adams DS (1992). Mechanisms of cell shape change: the cytomechanics of cellular response to chemical environment and mechanical loading. *J Cell Biol* **117**, 83–93.

Butt H-J & Jaschke M (1995). Calculation of thermal noise in atomic force microscopy. *Nanotechnology* **6**, 7.

Costa KD (2003). Single-cell elastography: probing for disease with the atomic force microscope. *Dis Markers* **19**, 139–154.

De Deyne PG (2001). Application of passive stretch and its implications for muscle fibres. *Phys Ther* **81**, 819–827.

Dowling EP, Ronan W, Ofek G, Deshpande VS, McMeeking RM, Athanasiou KA & McGarry JP (2012). The effect of remodelling and contractility of the actin cytoskeleton on the shear resistance of single cells: a computational and experimental investigation. *J R Soc Interface* **9**, 3469–3479.

Ersoy I, Bunyak F, Palaniappan K, Sun M & Forgacs G (2008). Cell spreading analysis with directed edge profile-guided level set active contours. *Med Image Comput Comput Assist Interv* **11**, 376–383.

Fletcher DA & Mullins RD (2010). Cell mechanics and the cytoskeleton. *Nature* **463**, 485–492.

Gunst SJ & Zhang W (2008). Actin cytoskeletal dynamics in smooth muscle: a new paradigm for the regulation of smooth muscle contraction. *Am J Physiol Cell Physiol* **295**, C576–C587.

Hale NA, Yang Y & Rajagopalan P (2010). Cell migration at the interface of a dual chemical-mechanical gradient. *ACS Appl Mater Interfaces* **2**, 2317–2324.

Hassani H (2007). Singular spectrum analysis: Methodology and comparison. *J Data Sci* **5**, 8.

Hong Z, Ersoy I, Sun M, Bunyak F, Hampel P, Hong Z, Sun Z, Li Z, Levitan I, Meininger GA & Palaniappan K (2013). Influence of membrane cholesterol and substrate elasticity on endothelial cell spreading behavior. *J Biomed Mater Res A* **101**, 1994–2004.

Hong Z, Sun Z, Li Z, Mesquitta WT, Trzeciakowski JP & Meininger GA (2012). Coordination of fibronectin adhesion with contraction and relaxation in microvascular smooth muscle. *Cardiovasc Res* **96**, 73–80.

Hutter JL & Bechhoefer J (1993). Calibration of atomic-force microscope tips. *Rev Sci Instrum* **64**, 6.

Imtiaz MS, von der Weid P-Y & van Helden DF (2010). Synchronization of Ca^{2+} oscillations: a coupled oscillator-based mechanism in smooth muscle. *FEBS J* **277**, 278–285.

Jülicher F & Prost J (1997). Spontaneous oscillations of collective molecular motors. *Phys Rev Lett* **78**, 4510–4513.

Karlon WJ, Hsu PP, Li S, Chien S, McCulloch AD & Omens JH (1999). Measurement of orientation and distribution of cellular alignment and cytoskeletal organization. *Ann Biomed Eng* **27**, 712–720.

Kim HR, Gallant C, Leavis PC, Gunst SJ & Morgan KG (2008). Cytoskeletal remodelling in differentiated vascular smooth muscle is actin isoform dependent and stimulus dependent. *Am J Physiol Cell Physiol* **295**, C768–C778.

Kim T-J, Seong J, Ouyang M, Sun J, Lu S, Hong JP, Wang N & Wang Y (2009). Substrate rigidity regulates Ca^{2+} oscillation via RhoA pathway in stem cells. *J Cell Physiol* **218**, 285–293.

Koenderink GH, Dogic Z, Nakamura F, Bendix PM, MacKintosh FC, Hartwig JH, Stossel TP & Weitz DA (2009). An active biopolymer network controlled by molecular motors. *Proc Natl Acad Sci U S A* **106**, 15192–15197.

Kruse K & Jülicher F (2005). Oscillations in cell biology. *Curr Opin Cell Biol* **17**, 20–26.

Lehenkari PP & Horton MA (1999). Single integrin molecule adhesion forces in intact cells measured by atomic force microscopy. *Biochem Biophys Res Commun* **259**, 645–650.

Li QS, Lee GY, Ong CN & Lim CT (2008). AFM indentation study of breast cancer cells. *Biochem Biophys Res Commun* **374**, 609–613.

Mardia KV & Jupp P (2000). *Directional Statistics (2nd edition)*. John Wiley and Sons Ltd.

Martens JC & Radmacher M (2008). Softening of the actin cytoskeleton by inhibition of myosin II. *Pflugers Arch* **456**, 95–100.

Martinez-Lemus LA, Hill MA, Bolz SS, Pohl U & Meininger GA (2004). Acute mechanoadaptation of vascular smooth muscle cells in response to continuous arteriolar vasoconstriction: implications for functional remodelling. *FASEB J* **18**, 708–710.

Martinez-Lemus LA, Hill MA & Meininger GA (2009). The plastic nature of the vascular wall: a continuum of remodelling events contributing to control of arteriolar diameter and structure. *Physiology (Bethesda)* **24**, 45–57.

Otsu N (1979). A threshold selection method from gray-level histograms. *IEEE Trans Syst Man Cybern* **9**, 62–66.

Parker CA, Takahashi K, Tang JX, Tao T & Morgan KG (1998). Cytoskeletal targeting of calponin in differentiated, contractile smooth muscle cells of the ferret. *J Physiol* **508**, 187–198.

Plaçais PY, Balland M, Guerin T, Joanny JF & Martin P (2009). Spontaneous oscillations of a minimal actomyosin system under elastic loading. *Phys Rev Lett* **103**, 158102.

Poythress RH, Gallant C, Vetterkind S & Morgan KG (2013). Vasoconstrictor-induced endocytic recycling regulates focal adhesion protein localization and function in vascular smooth muscle. *Am J Physiol Cell Physiol* **305**, C215–C227.

Qiu H, Zhu Y, Sun Z, Trzeciakowski JP, Gansner M, Depre C, Resuello RRG, Natividad FF, Hunter WC, Genin GM, Elson EL, Vatner DE, Meininger GA & Vatner SF (2010). Short Communication: Vascular smooth muscle cell stiffness as a mechanism for increased aortic stiffness with aging. *Circ Res* **107**, 615–619.

Rex CS, Chen LY, Sharma A, Liu J, Babayan AH, Gall CM & Lynch G (2009). Different Rho GTPase-dependent signaling pathways initiate sequential steps in the consolidation of long-term potentiation. *J Cell Biol* **186**, 85–97.

Ruiz JP, Pelaez D, Dias J, Ziebarth NM & Cheung HS (2012). The effect of nicotine on the mechanical properties of mesenchymal stem cells. *Cell Health Cytoskelet* **4**, 29–35.

Schillers H, Walte M, Urbanova K & Oberleithner H (2010). Real-time monitoring of cell elasticity reveals oscillating myosin activity. *Biophys J* **99**, 3639–3646.

Sehgel NL, Zhu Y, Sun Z, Trzeciakowski JP, Hong Z, Hunter WC, Vatner DE, Meininger GA & Vatner SF (2013).

Increased vascular smooth muscle cell stiffness: a novel mechanism for aortic stiffness in hypertension. *Am J Physiol Heart Circ Physiol* **305**, H1281–H1287.

Staiculescu MC, Galinanes EL, Zhao G, Ulloa U, Jin M, Beig MI, Meininger GA & Martinez-Lemus LA (2013). Prolonged vasoconstriction of resistance arteries involves vascular smooth muscle actin polymerization leading to inward remodelling. *Cardiovasc Res* **98**, 428–436.

Sun Z, Martinez-Lemus LA, Hill MA & Meininger GA (2008). Extracellular matrix-specific focal adhesions in vascular smooth muscle produce mechanically active adhesion sites. *Am J Physiol Cell Physiol* **295**, C268–C278.

Sun Z, Martinez-Lemus LA, Trache A, Trzeciakowski JP, Davis GE, Pohl U & Meininger GA (2005). Mechanical properties of the interaction between fibronectin and $\alpha_5\beta_1$-integrin on vascular smooth muscle cells studied using atomic force microscopy. *Am J Physiol Heart Circ Physiol* **289**, H2526–H2535.

Sweeney HL & Houdusse A (2010). Myosin VI rewrites the rules for myosin motors. *Cell* **141**, 573–582.

Tsien RW & Tsien RY (1990). Calcium channels, stores, and oscillations. *Annu Rev Cell Biol* **6**, 715–760.

Uhlén P & Fritz N (2010). Biochemistry of calcium oscillations. *Biochem Biophys Res Communs* **396**, 28–32.

Végh AG, Fazakas C, Nagy K, Wilhelm I, Krizbai IA, Nagyőszi P, Szegletes Z & Váró G (2011). Spatial and temporal dependence of the cerebral endothelial cells elasticity. *J Mol Recognit* **24**, 422–428.

Woolner S & Bement WM (2009). Unconventional myosins acting unconventionally. *Trends Cell Biol* **19**, 245–252.

Zemel A, Rehfeldt F, Brown AE, Discher DE & Safran SA (2010). Optimal matrix rigidity for stress fibre polarization in stem cells. *Nat Phys* **6**, 468–473.

Zhu Y, Qiu H, Trzeciakowski JP, Sun Z, Li Z, Hong Z, Hill MA, Hunter WC, Vatner DE, Vatner SF & Meininger GA (2012). Temporal analysis of vascular smooth muscle cell elasticity and adhesion reveals oscillation waveforms that differ with aging. *Aging Cell* **11**, 741–750.

Additional information

Competing interests

None declared.

Author contributions

The work presented in this paper was undertaken in the laboratories in Dalton Cardiovascular Research Centre at the University of Missouri located in Columbia, Missouri, USA. Z.H., Z.S. and G.A.M. designed experiments; Z.H., M.L. and Z.L. conducted experiments; Z.H., M.L, F.B., I.E., J.P.T., M.J., K.P. and G.A.M. designed and/or wrote analysis algorithms and analysed data; Z.H., Z.S., M.L, M.C.S., M.J., L.M.-L., J.P.T., M.A.H. and G.A.M contributed to data interpretation; Z.H., Z.S., M.L., F.B., J.P.T., M.C.S., L.M-L., M.A.H., K.P. and G.A.M wrote, reviewed and edited the manuscript as well as helped respond to the reviewers. All authors read and approved this manuscript.

Funding

This work was supported by NIH grant P01HL095486 to G.A.M. and partially supported by NIH grant R33EB00573 to K.P.

Acknowledgements

None declared.